Chemical Design of IrS 2 Polymorphs to Understand the Charge/Discharge Asymmetry in Anionic Redox Systems

Thomas Marchandier, Sathiya Mariyappan, Artem Abakumov, Stéphane Jobic, Bernard Humbert, Jean-Yves Mevellec, Gwenaëlle Rousse, Maxim Avdeev, Rémi Dedryvère, Dominique Foix, et al.

Chemical design of IrS_2 polymorphs to understand charge/discharge asymmetry in anionic redox systems

Thomas Marchandier,[1,2,3] Sathiya Mariyappan,[1,2] Artem M. Abakumov,[4] Stéphane Jobic,[5] Bernard Humbert,[5] Jean-Yves Mevellec,[5] Gwenaëlle Rousse,[1,2,3] Maxim Avdeev,[6,7] Rémi Dedryvère,[2,8] Dominique Foix, [2,8] Antonella Iadecola,[2] Marie Liesse Doublet[2,9] and Jean-Marie Tarascon[1,2,3,*]

1. Collège de France, Chaire de Chimie du Solide et de l'Energie, UMR 8260, 11 place Marcelin Berthelot, 75231 Paris Cedex 05, France
2. Réseau sur le Stockage Electrochimique de l'Energie (RS2E), FR CNRS 3459, 75005 Paris, France
3. Sorbonne Université− 4 place Jussieu, F-75005 Paris, France
4. Center for Energy Science and Technology, Skolkovo Institute of Science and Technology, 3 Nobel Street, Moscow, 121205, Russia
5. Université de Nantes, CNRS, Institut des Matériaux Jean Rouxel, IMN, F-44000, Nantes, France
6. School of Chemistry, the University of Sydney, Sydney, NSW 2006, Australia
7. Australian Centre for Neutron Scattering, Australian Nuclear Science and Technology Organisation, New Illawarra Rd, Lucas Heights, NSW 2234, Australia
8. IPREM, CNRS, Université de Pau & Pays Adour, E2S-UPPA, Hélioparc, 2 Avenue P.Angot, 64053 Pau Cedex 9, France
9. Institut Charles Gerhardt, Université de Montpellier-CNRS-ENSCM, Place Eugène Bataillon, 34095 Montpellier, France

Abstract:

Li-ion batteries are growing in demands and such growth calls for the quest of high energy density electrode materials. Li-rich layered oxides that show both cationic and anionic redox are expected to meet the high energy requirement. However, the oxygen anion activity triggers numerous structural and electronic rearrangements that need to be understood prior envisioning applications. Here, we chemically design two new Li_xIrS_2 polymorphs to interrogate further the mechanisms of the ligand redox process. By combined structural and spectroscopic characterizations we show that electrochemical lithiation/ delithiation of the polymorphs involve different sulfur redox couples that stands as an unusual behavior. These structure dependent kinetic pathways lead to ~1 V difference between the two polymorphs, hence providing the missing link between structure and hysteresis in anionic redox systems. These insights on the origin of hysteresis can guide proper parameters to cure it hence laying the ground work for the design of new practical electrode materials.

Introduction:

Energy storage represents one of the main challenges to achieve a viable transition from fossil fuels to renewable energy resources (solar, wind, etc…) which are green but intermittent. Hopes were placed in the lithium-ion technology that has conquered both the portable devices and electric vehicles markets.[1] However, the energy density of these devices has to be improved. Targeting this goal, among many recent developments, one strategy has been devoted to Li-rich layered oxides $Li_{1+x}M_{1-x}O_2$ (where M stands for transition metal ion(s)) with reversible capacities exceeding 250 $mAh.g^{-1}$. The materials were characterized by high valent redox in which either cation or anion or both oxidize to unusually high oxidation states.[2–4] Nevertheless, the activation of such high valent redox process - more specifically with anions - come with its own complexification affecting the cycling of these materials, in particular by exhibiting voltage hysteresis and voltage fade upon cycling. The future of these cathode materials is therefore directly linked to a fundamental solid-state chemistry study on charge compensation mechanisms.

The understanding of voltage hysteresis is particularly important because it questions the symmetry of redox processes between charge and discharge. Yet, no common consensus has been reached yet on its origin and interplay with the structural and electronic aspects of the cathode material.[4] According to numerous authors,[5–7] this phenomenon would result from the lithium sites diversification induced by the pseudo-reversible cation migration differentiating the charge from the discharge. Although alluring, this scenario is challenged by systems where in spite of a fast and highly reversible cation migration the hysteresis is still preserved. Therefore, other studies have proposed that the origin of hysteresis could arise from O-O dimers whose formation and rupture would follow distinct reaction pathways.[8,9] However, all these mechanisms are based on the complex interpretation of various ex situ and operando spectroscopic techniques that barely lead to unanimous conclusions especially on the nature of the anionic oxidized species (dimers for instance). In addition, the experimental bottlenecks to ensure the homogeneity of the electrochemically-made materials, overcome difficulties in accessing the bulk properties and to quantify the cation migration and/ or dimer formation, complicate further exploration of the phenomenon.

One naive idea to clarify the reaction asymmetry upon cycling would be to study simple systems where migrated cations or anionic dimers could be clearly stabilized and identified. However, finding these compounds among the oxide family is a brainteaser[10] that can be partially alleviated by moving to sulfides. Indeed, although less explored in the battery field than oxides due to lower energy densities, transition metal sulfides are known for decades to be able to stabilize S-S bonds.[11–14] However,

transition metal sulfides containing dimers are mainly found in pyrite or marcasite crystal structures, which do not have the proper open framework for topotactic insertion/de-insertion reactions. Consequently, lithium insertion in such phases (eg., FeS_2) induces large structural changes and loss of long-range order[15–17] that complicate the understanding of the structure/electrochemistry interactions. Further digging into the literature, the iridium sulfides got our attention. Indeed, Jobic and coworkers described in 1990[11] IrS_2 (termed hereafter as Jobic's IrS_2 or J-IrS_2), a compound combining both sulfur dimers[18] and a ramsdellite-like open framework suitable for the lithium topotactic insertion. Moreover, intrigued by the possibility to form lithiated iridium sulfides, we managed to stabilize a high temperature $LiIrS_2$ phase isostructural to $LiTiS_2$. Interestingly ~~whereas~~ $LiIrS_2$ (referred hereafter as Layered-$LiIrS_2$ or L-$LiIrS_2$) shares with, lithium rich layered oxides pristine a layered structure, whereas IrS_2 can mimic the charged layered material reported in literature with its open structure and S-S dimers. Therefore, the L-$LiIrS_2$/J-IrS_2 couple constitutes a suitable playground to study the redox process asymmetry between charge and discharge in anionic redox systems.

In this study, we report the behavior of the L-$LiIrS_2$/J-IrS_2 system through lithium insertion/de-insertion. Surprisingly, in spite of similar chemical compositions, these two materials show drastically different electrochemical behaviors. By combining diffraction investigations (synchrotron X-ray diffraction (SXRD), neutron powder diffraction (NPD)) with atomic resolution transmission electron microscopy and spectroscopic analyses (Ir-L_3-edge X-ray absorption spectroscopy (XAS), X-ray photoemission spectroscopy (XPS) and Raman spectroscopy), we demonstrate that the lithiation reaction in both systems proceeds through different structural and electronic pathways. This study points out the implications of the structure and of the dimers upon reaction pathways, it gives then clues to better understand the voltage asymmetry between charge and discharge in anionic redox systems.

Experimental:

Synthesis: The synthesis of **J-IrS_2** was performed following a previously reported protocol.[11] In a typical synthesis, about 200 mg of IrS_2 phase was obtained by mixing in an Ar-filled glovebox, iridium powder (99.8 % Alfa Aesar) and elemental sulfur (99.998 % Sigma-Aldrich) in a 1:2.1 molar ratio. The homogeneously hand grinded mixture was then transferred into a carbon coated quartz ampoule and subsequently sealed under dynamic vacuum (~10^{-3} mbar). Finally, the tubes were annealed in a muffle furnace at 930°C for 60 hrs and the product was recovered and stored in Ar-filled glove box.

A similar solid-state procedure was followed to synthetize **L-$LiIrS_2$**. In an Ar-filled glovebox, iridium powder, elemental sulfur and lithium sulfide (99.9 % Alfa Aesar) were mixed in a 1:1.5:0.55 ratio. The mixture was then annealed under vacuum in a sealed quartz ampoule (prepared following the same procedure described above) for 60 hrs at 700 °C.

The samples for ex-situ analyses of **L-IrS_2** were prepared by chemical delithiation of L-$LiIrS_2$, by mixing in an Ar-filled glovebox one equivalent of L-$LiIrS_2$ with two equivalents of iodine (99+ % Alfa Aesar). The mixture was then transferred in a quartz ampoule, sealed under vacuum and subsequently annealed for 12hrs at 150°C. After the reaction, the ampoule was opened under inert atmosphere and the powder was washed with dry acetonitrile to remove excess LiI and I_2 before being dried under vacuum.

Both a chemical and an electrochemical procedure have been attempted to prepare **J-$Li_{0.5}IrS_2$** ex-situ samples. For the first one, about 500 mg of J-IrS_2 and five equivalents of n-Butyl lithium (n-BuLi; 1.6 M in hexane, Sigma-Aldrich) were mixed together in a 40 mL glass vial under Ar-atmosphere and stirred for 5 hours. The resulting powder was thoroughly rinsed with hexane to remove the n- BuLi before being dried under vacuum. To prepare the lithiated J-Li_xIrS_2 phases electrochemically, an electrode was first prepared by mixing 500 mg of IrS_2 with 20 % (in mass) of Carbon-SP, and was then discharged galvanostatically (constant current mode) at C/50 rate vs Li metal in a home-made Swagelok type cell using LP-30 (1M $LiPF_6$ in 1:1 by volume mixture of EC- DMC; bought from Dodochem, China) as electrolyte. The lithiated powder was then collected from the electrochemical cell under inert atmosphere and washed three times with DMC before being dried under vacuum.

X-ray and neutron diffraction: Synchrotron X-ray powder diffraction (SXRD) patterns were measured at the 11-BM beamline of the Advanced Photon Source (Argonne National Laboratory) with λ = 0.45789 Å. The different powders were mixed with an appropriate amount of dried amorphous silica (to limit the absorption) in an Ar-filled glovebox before being sealed in glass capillaries of 0.6 mm in diameter. Operando powder X-ray diffraction (XRD) experiments were performed using a homemade airtight electrochemical cell[19] equipped with a Be window, assembled under argon filled glovebox and the patterns were collected in Bragg−Brentano geometry with a Bruker D8 Advance diffractometer supplied with a Cu K_α X-ray source (λ_1 = 1.5406 Å, λ_2= 1.5444 Å) and a LynxEye XE detector. Constant wavelength neutron powder diffraction (NPD) data were collected at room temperature on the WOMBAT high-intensity neutron powder diffractometers using the wavelength of 1.54183 Å.[20] To prevent reaction of the samples with ambient atmosphere, the samples were loaded into 9 mm diameter cylindrical vanadium cans in Ar glove box and sealed with an indium wire. All diffraction patterns were Rietveld refined using the FullProf program[21].

Bond valence energy landscape (BVEL) calculations were done with the BondSTR program implemented in the FullProf Suite following the method developed by Adams.[22,23]

Electrochemical measurements: Swagelok-type cells were assembled using a lithium metal disk as the negative electrode and composite positive electrodes made by hand milling either J-IrS_2 or L-$LiIrS_2$ with

20 % in mass carbon Super P. Both positive and negative electrodes were parted by a Whatmann GF/D borosilicate glass fibers sheets soaked in an electrolyte composed of a mixture of EC/DMC (1:1) with 1 M $LiPF_6$ (LP-30). The cells were assembled in an argon-filled glovebox and cycled at C/20 rate (1C= current to remove 1 lithium) in a Biologic galvanostat/ potentiostat (MPG-2/ VMP-3) using constant current (galvanostatic) mode.

Microscopy: Samples for transmission electron microscopy (TEM) were prepared in an Ar-filled glove box by crushing the crystals in a mortar in dry DMC and depositing drops of suspension onto holey carbon grids. The samples were transported to the microscope column avoiding contact with air. Electron diffraction (ED) patterns, high angle annular dark field scanning transmission electron microscopy (HAADF-STEM) images and differential phase contrast (dDPC-STEM) images were obtained with an aberration-corrected Titan Themis Z electron microscope operated at 200 kV.

X-ray photoemission spectroscopy: X-ray photoemission spectroscopy (XPS) measurements were carried out with a THERMO Escalab spectrometer, using focused monochromatic Al Kα radiation (hν = 1486.6 eV) and equipped with an argon-filled glove box allowing to preserve the samples from moisture and air at all times from their preparation to their analysis. Peaks were recorded with constant pass energy of 20 eV. The pressure in the analysis chamber was around 5×10^{-8} mbar. The binding energy scale was calibrated using the C 1s peak at 285.0 eV from the hydrocarbon contamination present at the samples surface. The spectra were fitted using a minimum number of components. Several spectra were recorded at different times to check that the samples were not subjected to degradation during the X-ray irradiation.

X-Ray absorption spectroscopy (XAS): Ex situ XAS measurements at the Ir L3-edge were performed in transmission mode at the ROCK beamline[24] of synchrotron SOLEIL (France). A Si(111) channel-cut quick-XAS monochromator with an energy resolution of 1.1 eV at 11 keV was used. The intensity of the monochromatic X-ray beam was measured with three consecutive ionization chambers filled with 40 mL of N_2. A pellet of α-Li_2IrO_3 was placed between the second and the third ionization chamber to ensure the energy calibration. For each compound, 8 mm diameter pellet was prepared in an Ar-filled glovebox by mixing 5 mg of sample with almost 30 mg of dried cellulose, embedded in kapton tape and sealed in plastic bag to avoid any air exposure during the XAS measurements. The data was treated using the Demeter package for energy calibration and normalization.[25] The EXAFS oscillations of the L-IrS_2 compound were fitted using the Artemis software. The Fourier transforms of EXAFS oscillations were carried out in k-range from 3.5 $Å^{-1}$ to 15.9 and the fitting was performed in R-range from 1.0 to 3.9 Å using k^3 weight. EXAFS amplitudes and phase-shifts were calculated by FEFF7 with a starting

model derived from XRD and ND (Table S8). Except the radial distance (R) and the Debye-Waller factor (σ^2), all other parameters were kept constant (N_i, E_0, S_0^2) in the conventional least squares modelling using the phase and amplitude factors calculated by the FEFF7.

Raman spectroscopy: Raman spectra were collected with a Renishaw's InVia Reflex Raman system using a microscope confocal InVia Reflex device. The instrument was equipped with a double edge filter to eliminate the Rayleigh scattering, and with a CCD camera working at a temperature of 220 K with a 1024 X 256 pixels array. Laser excitations were at 488 nm, 514 nm, 633 nm and 785 nm. Only the excitation at 785 nm enabled us to record the spectra of all the samples without destroying them and without making them evolve under a laser. The setup was composed of a confocal microscope that was equipped with an automated XYZ table allowing us to position the capillaries containing the samples away from the environment in the focal plane of the optical microscope. The spectral resolution achieved with the use of gratings of 2400 or 1200 grooves per mm was between 3 and 5 cm^{-1} depending on the excitation wavelength. The focused power of the laser beam on the powders inside the capillaries was also checked for each wavelength to avoid any transformation or heating of the samples. Accordingly, the surface power density was kept below 15 $\mu W\ \mu m^{-2}$ with the magnitudes 50X of the long distance working objective being selected after a series of tests.

Magnetic properties: The evolution of the magnetic susceptibility with temperature was measured using a SQUID (XL, Quantum Design), under zero field cooled (ZFC) conditions between 2 K and 400 K with an applied magnetic field of 10 kOe.

Results:

A) Crystal structure of the pristine materials

Both J-IrS_2 and L-$LiIrS_2$ were synthesized at high temperature by mixing the required precursors (iridium metal, sulfur powder and Li_2S) inside vacuum-sealed quartz tubes as described in the experimental part. The structural analyses of both materials were carried out by combined synchrotron X-ray and neutron powder diffraction pattern as well as high-resolution transmission electron microscopy analyses. The results obtained for J-IrS_2 are represented in Figure 1. The Rietveld refinement of both synchrotron X-ray and neutron powder diffraction patterns (cf. figure 1 a and b) combined with electron diffraction patterns (cf. figure 1e and S1) confirmed the previously reported orthorhombic (*Pnma, a* = 19.8201(2) Å, *b* = 3.5736(2) Å, c = 5.6339(2) Å) structural model for J-IrS_2 (cf. figure 1 c and Table S1).[11] In this structure, iridium atoms are octahedrally coordinated to sulfur and the formed IrS_6 octahedra share corners and edges to produce rutile-type [1x1] and ramsdellite-type [2x2] channels. A closer look into the structure, especially through dDPC-STEM picture (cf. figure 1 d), reveals that the

[1x1] channels of J-IrS_2 are distorted leading to short S-S distances of around 2.27 Å. Former Raman spectroscopy of this phase has unambiguously attributed these short distances to the presence of S_2^{2-} dimers in the structure.[18] Conversely, the [2x2] ramsdellite-like channels demonstrate no signs of distortion and can be ideal sites to host small cations as already demonstrated in structurally related MnO_2 polymorph.[26]

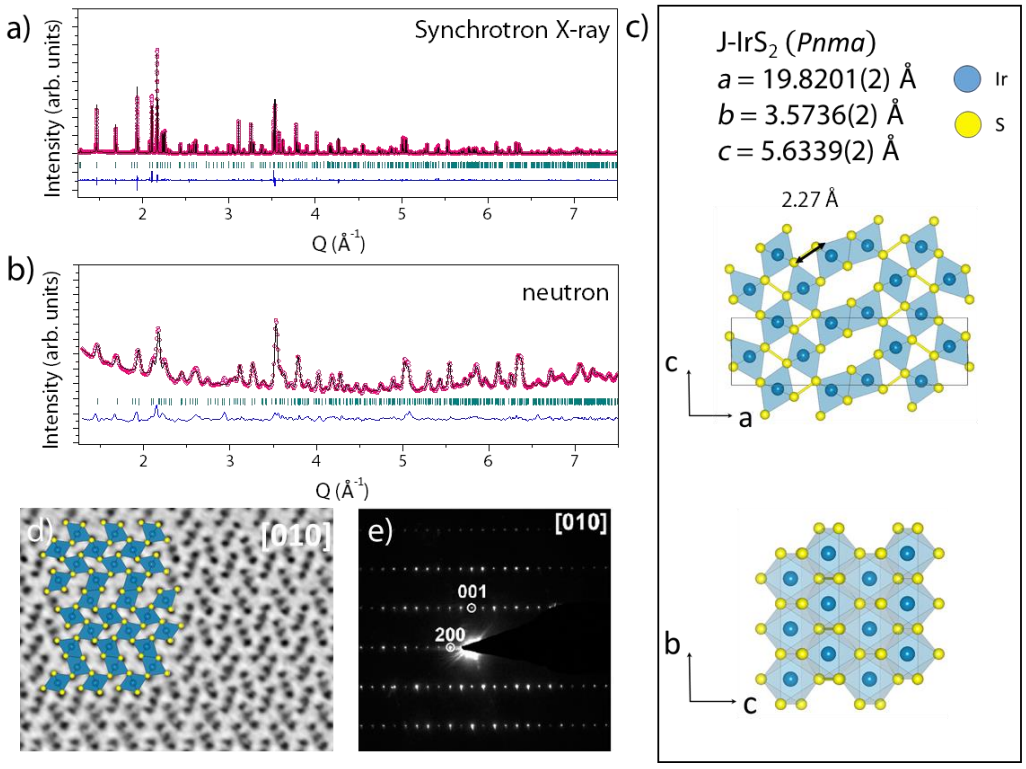

Figure 1: (a) Synchrotron X-ray and (b) neutron Rietveld refinements of J-IrS_2 at 300 K. Wavelengths for synchrotron X-ray and neutron are λ = 0.45789 Å and λ = 1.54183 Å, respectively. The pink circles, black continuous line, and bottom blue line represent the observed, calculated, and difference patterns, respectively. Vertical green tick bars stand for the Bragg positions. Associated crystallographic data are summed up in Table S1. (c) Structure of J-IrS_2 at 300 K. (d) [010] dDPC-STEM image of J-IrS_2 with the overlaid positions of the Ir and S atoms. (e) Corresponding electron diffraction pattern of J-$LiIrS_2$.

In contrast, the L-$LiIrS_2$ polymorph, not reported so far to the best of our knowledge, adopts the structure displayed in figure 2. Its X-ray synchrotron powder diffraction pattern was first indexed using the DICVOL software[27,28] in a trigonal unit cell (a = 3.5955(2) Å, c = 5.6749(4) Å) and this indexation was confirmed by electron diffraction pattern shown in Figure 2d. The similarities of this unit cell with the well-known layered transition metal chalcogenides led us to consider a structural model similar to the $LiTiS_2$ one ($P\bar{3}m1$) which was further validated by both SXRD and neutron powder diffraction refinements (cf. figure 2 a and b and Table S2). In this structure, iridium atoms sit in the centres of regular IrS_6 octahedra sharing edges with each other to form CdI_2-like layers stacked along the **c**

direction (cf. figure 2c) , as also confirmed by the EXAFS analysis (see table S3). The HAADF-STEM image (figure 2e) clearly shows that the iridium atoms from one layer to another are aligned orthogonally to the layer plane. Such a stacking is referred as O1 according to Delmas nomenclature[29] as the Li atoms are in octahedral position and the unit cell contains one MS_2 layer. The determination of the exact Li/Ir ratio with Inductively Coupled Plasma Mass Spectrometry (ICP-MS) was complicated by the insolubility of the material even in strong acidic solutions. Nevertheless, HAADF-STEM pictures show closing loops formed by the IrS_2 layers at the edge of the crystallites that could indicate a relative densification of the material on the surface hence the formation of slightly lithium deficient phase (Li_xIrS_2 where $x < 1$; $Li/Ir < 1$) ~~as~~ frequently observed with the synthesis of $LiMS_2$ compounds (ref).[30] This last assumption could also explain the c/a=1.58 ratio observed for this compound significantly smaller than the one observed in $LiTiS_2$ or $LiVS_2$ (1.80)

Overall, structural analyses indicate that both J-IrS_2 and L-$LiIrS_2$ possess either tunnels or Van der Waals layers, respectively, hence suggesting their feasibility to reversibly uptake and release Li^+ ions as we explore next.

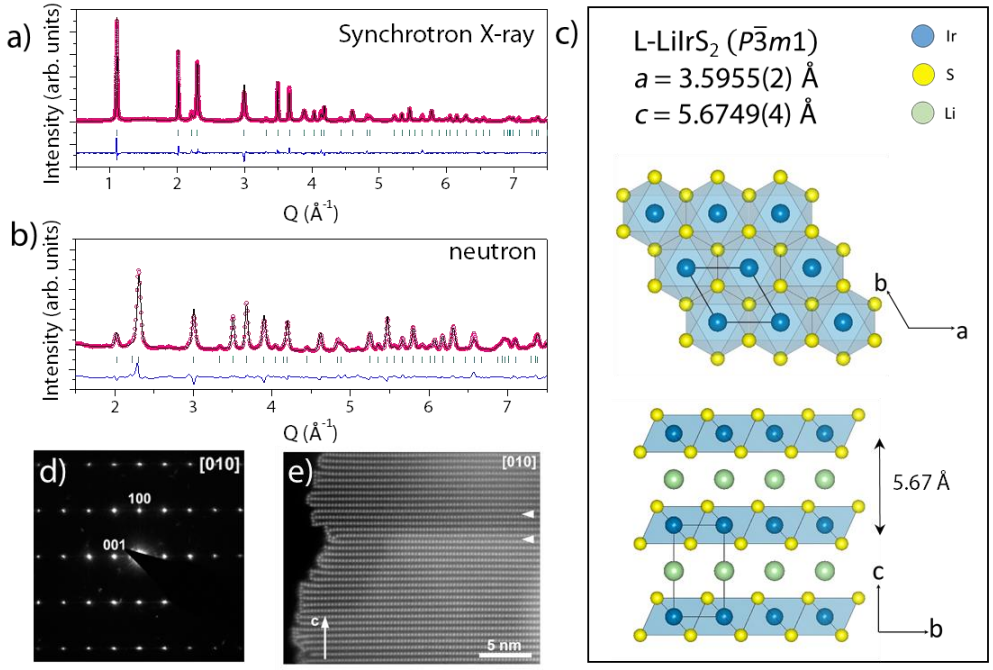

Figure 2: (a) Synchrotron X-ray and (b) neutron Rietveld refinements of L-$LiIrS_2$ at 300 K. Wavelengths for synchrotron X-ray and neutrons are λ = 0.45789 Å and λ = 1.54183 Å, respectively. The pink circles, black continuous line, and bottom blue line represent the observed, calculated, and difference patterns, respectively. Vertical green tick bars stand for the Bragg positions. Associated crystallographic data are summed up in Table S2. (c) Structure of L-$LiIrS_2$ at 300 K. (d) Electron diffraction pattern of L-$LiIrS_2$. (e) [010] HAADF-STEM image of L-$LiIrS_2$ showing the O1-type structure. Stacking faults are occasionally present and marked with arrowheads.

B) Electrochemical study

Li half-cells were assembled for both J-IrS_2 and L-$LiIrS_2$ using lithium metal as counter electrode and LP30 (1M $LiPF_6$ in 1:1 mixture of ethylene carbonate: dimethyl carbonate) as electrolyte. The cells were cycled between different voltage cut-off and potential ranges of 1.3 -3 V for J-IrS_2 and 1.7 -3.5 V for L-$LiIrS_2$. These specific conditions were fixed to avoid material degradation. The cells were cycled at a C/20 rate (1 Li per unit formula removed or inserted in 20 h). The composition vs voltage plots together with the corresponding derivative curves for the first cycle are shown in Figure 3.

For J-IrS_2, the insertion and de-insertion of lithium takes place through a plateau-like profile at 1.4 and 1.5 V vs. Li^+/Li^0 respectively. Out of the 0.5 lithium inserted into the structure only 0.3 is removed on subsequent charge. By pushing the reduction cut-off potential to lower voltages, a new insertion process appears at 1.15 V that accounts for the insertion of almost five lithium into the structure (cf. figure S2). However, this low voltage process is poorly reversible and accompanied by a high polarization and irreversibility on subsequent charge suggesting a possible conversion reaction (leading most likely to poorly crystalized Li_2S and Ir components).

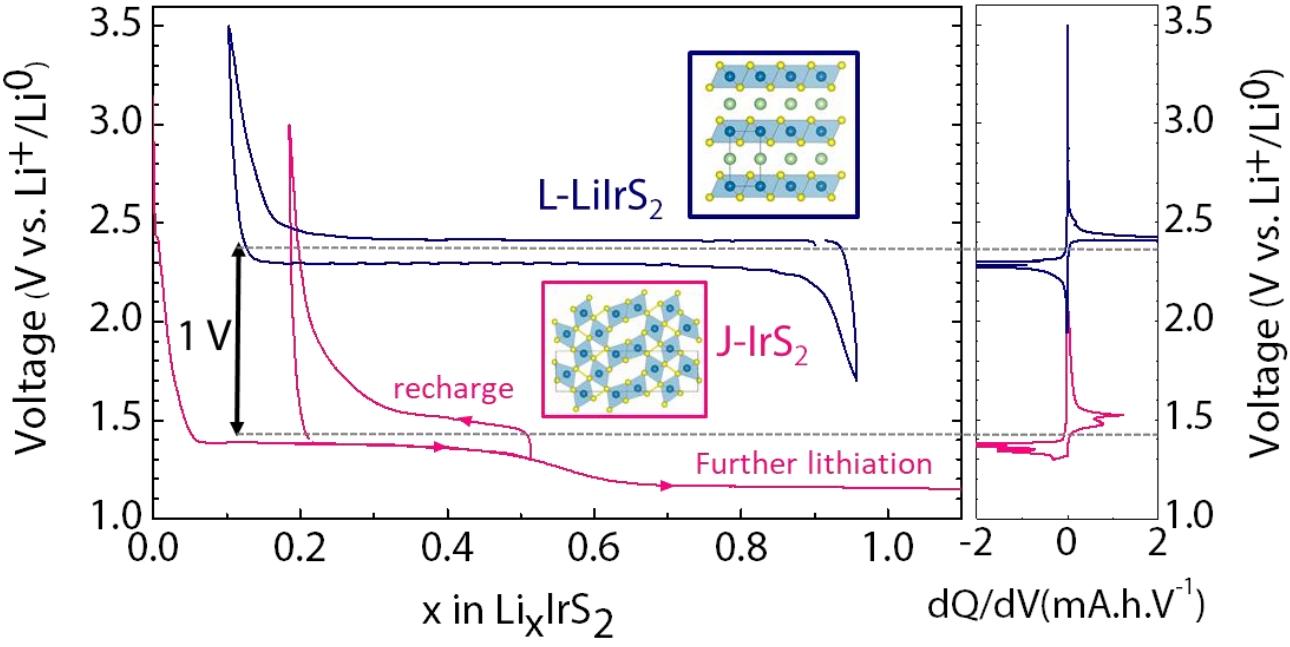

Figure 3: First cycle voltage–composition trace (left) and derivative curves (right) of L-$LirS_2$ (blue) and J-IrS_2 (pink) cycled at C/20. The starting composition of L-$LiIrS_2$ is considered as $Li_{0.9}IrS_2$ accounting for Li-deficiency as explained in the synthesis part. The arrows on the J-IrS_2 voltage curves indicate the cycling directions. The low voltage 1.15 V discharge of J-IrS_2 extends up to ~5 Li uptake and is not shown here for clarification purpose.

Turning to L-$LiIrS_2$, strikingly the de-insertion and insertion of Li^+ proceeds through a voltage plateau located 1V higher than for J-IrS_2 (cf. figure 3). Interesting as well is the feasibility to insert more Li^+ on

discharge (~0.9) that it has been removed on charge (~0.8). Such difference is not fortuitous but rather suggests, based on coulomb titration, that the pristine material is slightly Li deficient (L-$Li_{0.9}IrS_2$). To interrogate the origin of the 1 V difference, we next investigate the crystal structure evolution of the polymorphs during Li insertion/extraction.

Operando XRD analyses have been carried out for both J-IrS_2 and L-$LiIrS_2$ (cf. figure S3). Upon lithiation, J-IrS_2 exhibits biphasic process and a nearly single phase compound was reached for the composition J-$Li_{0.5}IrS_2$. Upon further lithiation of J-$Li_{0.5}IrS_2$, a new biphasic process starts to appear and progresses till 2 lithium consumption and fades away for greater amounts of reacted Li^+ ($2<x<5$) (cf. figure S4). Similarly, L-$LiIrS_2$ followed biphasic delithiation and lithiation processes where the delithiated L-Li_xIrS_2 also exhibited layered structure but full refinement requires a higher resolution than lab XRD. In order to further understand these structural evolutions, we studied next the single-phase compositions by combined synchrotron XRD and TEM analyses.

C) Structure of the lithiated/delithiated phases

The **lithiated J-$Li_{0.5}IrS_2$** phase for structural analyses was formed either electrochemically or chemically via the use of n-butyllithium (n-BuLi) as a reacting agent. The SXRD pattern shown in Figure 4a is nearly alike that of J-IrS_2 and refined using the *Pnma* structural model of J-IrS_2 but with larger lattice parameters (cf. figure 4b). The S-S distance is difficult to measure from XRD analyses, as the pattern is dominated by the iridium contribution, we examined the S-S distances using dDPC-STEM imaging (cf. figure 4c and d; corresponding ED pattern in figure S5). The measured S-S average distance of 2.32(5) Å in J-$Li_{0.5}IrS_2$ is only slightly longer than the 2.27 Å observed in the pristine material (cf. figure 1c), implying that the dimers are preserved during the reduction process. Finally, the bond valence energy landscape (BVEL) calculation using the refined structure indicates that the lithium atoms in the J-$Li_{0.5}IrS_2$ were localized in the octahedral voids of the ramsdelite-type motifs channels. Accordingly, the final structure for J-$Li_{0.5}IrS_2$ is derived as shown in Figure 4e.

Next, we analyzed the highly lithiated J-Li_xIrS_2 phase obtained by further reducing J-$Li_{0.5}IrS_2$ at 1.15 V. Although the XRD pattern showed at first sight similarities with the J-IrS_2 and J-$Li_{0.5}IrS_2$ XRD patterns, a direct extrapolation of the structure from these models was not successful. HAADF-STEM and dDPC-STEM experiments (cf. figure S6 and S7) were then carried out and permitted to build a structural model which was further confirmed by Rietveld refinement of the operando XRD pattern (*Pnma*, a = 23.0886(5) Å, b = 3.6257(2) Å, c = 5.6144(2) Å) (cf. figure S8 and Table S5). The obtained structure differs mainly from the J-IrS_2 and J-$Li_{0.5}IrS_2$ ones by a drastic elongation of the S-S distances previously engaged in the dimers bonding (cf. figure 4e) hence suggesting their breaking during the lithiation process. Structurally speaking and as supported by BVEL calculation, this structural relaxation frees the

rutile channels for lithium insertion. Therefore, assuming a complete filling of the octahedral vacant sites of the rutile and ramsdelite channels we propose the chemical formula J-LiIrS$_2$ for the phase lithiated to 1.15V. Lastly, HAADF-STEM pictures (cf. figure S6) confirmed that the presence of this phase comes along with amorphous phase, which support that a concomitant conversion reaction occurs together with the formation of J-LiIrS$_2$.

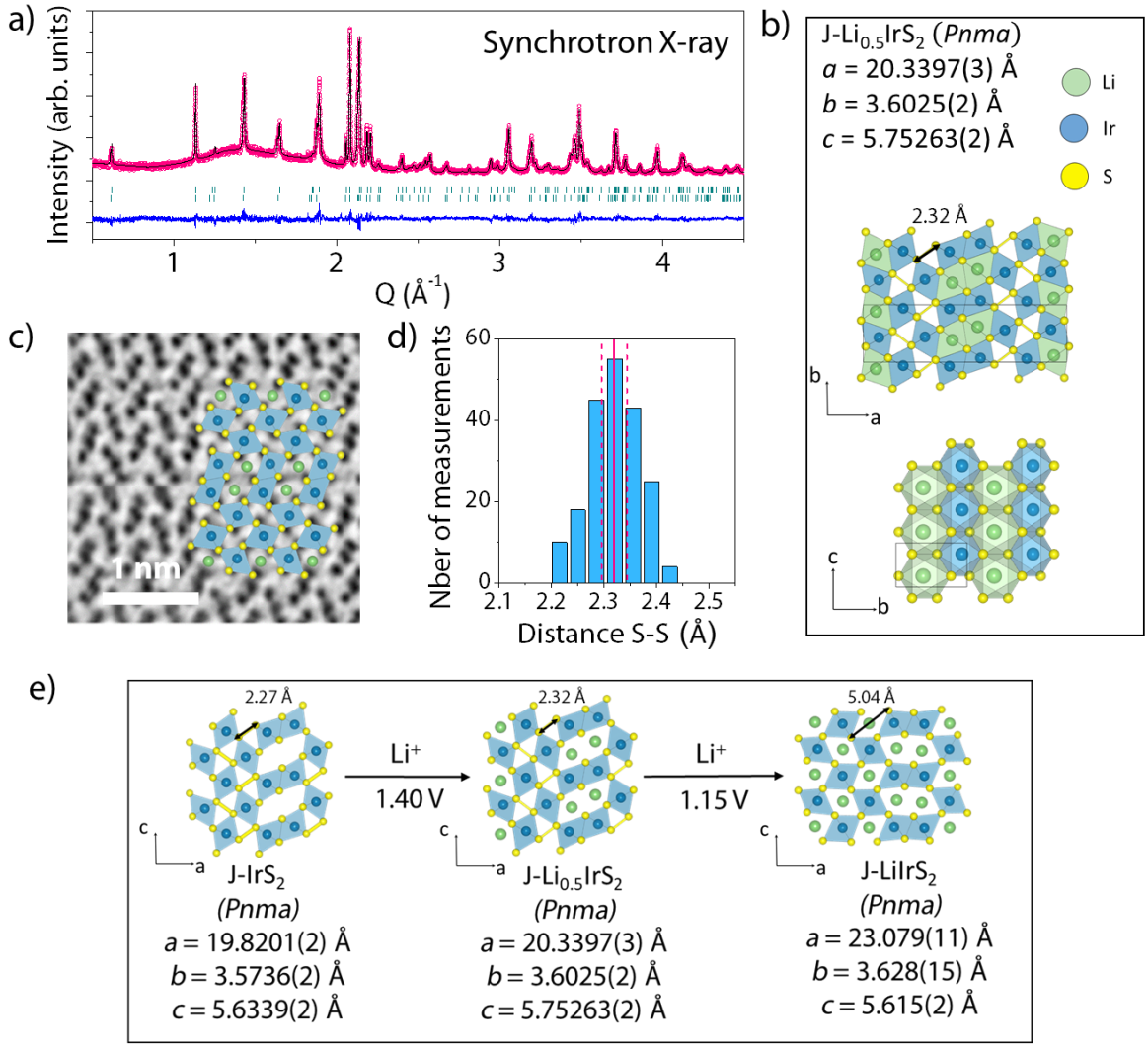

Figure 4: (a) Synchrotron X-ray Rietveld refinement of J-Li$_{0.5}$IrS$_2$ at 300 K. The wavelength for synchrotron X-ray is λ = 0.45789 Å. The pink circles, black continuous line, and bottom blue line represent the observed, calculated, and difference patterns, respectively. Vertical green tick bars stand for the Bragg positions. Two isostructural phases with small lattice parameters have been used to index the pattern and presence of two isostructural phases is expected to be linked with inhomogeneous lithiation of the J-IrS$_2$ particles. (b) Structure of J-Li$_{0.5}$IrS$_2$ at 300 K. c) [010] dDPC-STEM image of J-Li$_{0.5}$IrS$_2$ with the overlaid positions of the Li, Ir and S atoms. (d) Distribution of the S1-S3 (cf. tables S4) interatomic distances of the dimeric entities in the J-Li$_{0.5}$IrS$_2$ as measured from the [010] dDPC-STEM image. (e) Structural evolution of J-Li$_x$IrS$_2$ through lithiation. The Ir-S network structure of J-LiIrS$_2$ results directly from the structural relaxation of the Ir-S network of J-IrS$_2$ with the full disappearance of the S-S dimers.

Turning to the **delithiated L-Li_xIrS_2** phase (called hereafter L-IrS_2), it was obtained by chemical delithiation of L-$LiIrS_2$ with iodine in a sealed ampoule at 250 °C (cf. experimental section). Its composition $Li_{0.05}IrS_2$ was determined by ICP-MS measurements (cf. table S6). A first refinement was attempted using a layered structural model slightly distorted compared to the pristine one (*C*2/*m*, *a* = 5.6911(4) Å, *b* = 3.5450(3) Å, *c* = 5.2375(5) Å, β = 89.96(14)°). Although promising, this model could not properly reproduce the intensities of several peaks (cf. figure S9). Electron diffraction was then used to investigate the origin of the mismatch. It reveals the existence of a superstructure in this monoclinic model which corresponds to the **k** = [1/2 1/2 1/2] wave vector (cf. figure S10). In parallel, HAADF-STEM image (cf. figure 5f) has shown that the superstructure is caused by lateral displacements of the Ir atoms creating alternating short (~2.5 Å) and long (~3.2 Å) projected Ir-Ir distances along the Ir layers (cf. figure S11). The group theory distortion analysis lead to the construction of a triclinic super cell ($P\bar{1}$, *a* =3.3704(2) Å, *b* = 5.9622(10) Å, *c* = 6.2182(9) Å, α = 117.53(2)°, β = 103.792(9)°, γ = 93.865(4) °) and this model was finally confirmed by the Rietveld refinement of both L-IrS_2 synchrotron X-ray (cf. figure 5a) and neutron (cf. figure S12) powder diffraction patterns.

The obtained structure can be globally described as an O1 layered structure (cf. figure 5b and c and Table S7) with however noticeable distortion inside the layers. Thus, the IrS_6 coordination polyhedra are not any longer octahedra but rather square pyramids with 5 short Ir-S bonds with an average length of 2.38 Å and a longer one at 2.93 Å (cf. figure 5d). This feature is later confirmed with Ir-L-edge EXAFS (cf. figure 5e and table S8). From the atomic point of view, this distortion induces an Ir-Ir "dimerization" observed with HAADF-STEM (cf. figure 5f) while sulfur atoms are split into two different sites with very different environment (cf. figure S13). Indeed, while S1 (cf. table S7) positions are surrounded by three equidistant iridium atoms (Ir-S1≈ 2.3 Å), the S2 atoms develop similar short bonds with only two iridium atoms, the third neighbor being found at 2.93 Å. Bond valence calculations suggest that this environment difference could be the sign of a charge difference between the two sulfur atoms with the S1 position more negatively charged than S2. Such a transition metal (Ir-Ir) dimerization does not come as a total surprise since it has already been spotted and described in the low temperature $IrTe_2$ layered structure.[31–33] However, the origin of this distortion can be different from one compound to the other and will be detailed in the following section.

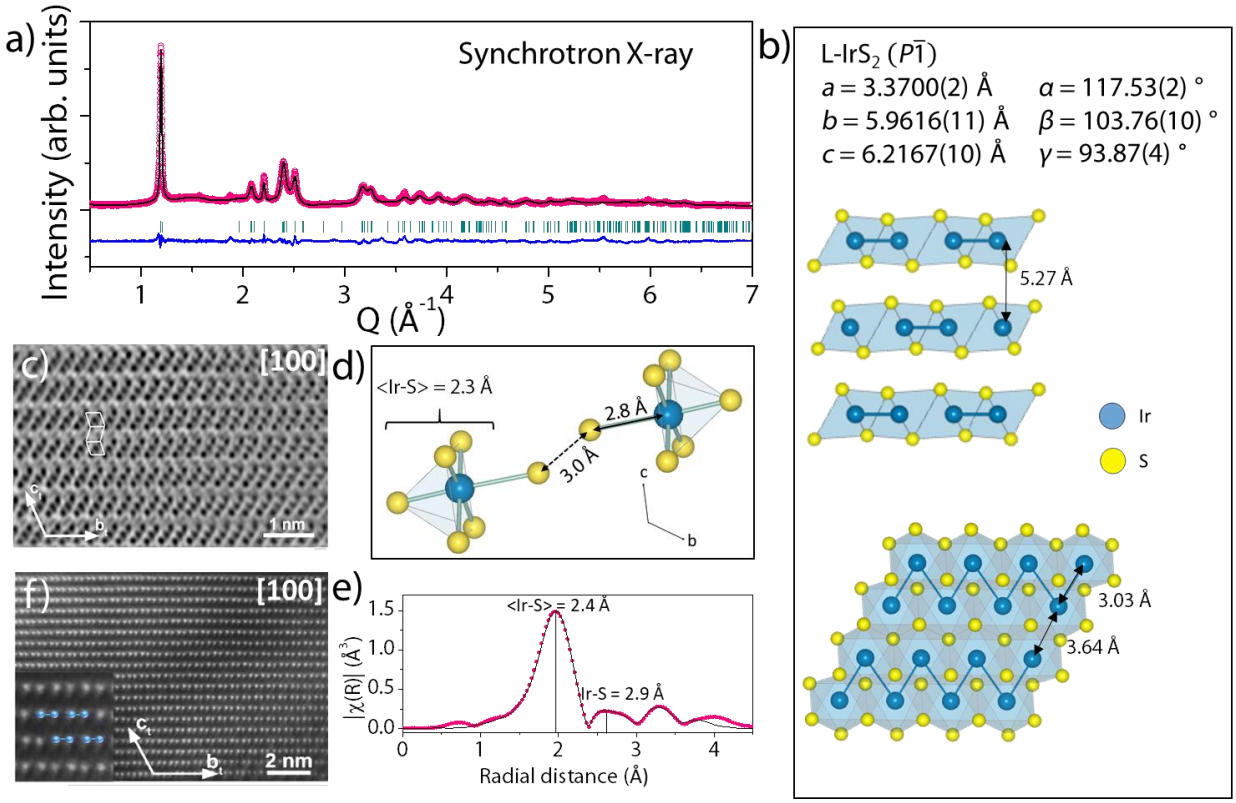

Figure 5: (a) Synchrotron X-ray Rietveld refinements of L-IrS_2 at 300 K. Wavelengths for synchrotron X-ray is λ = 0.45789 Å. The pink circles, black continuous line, and bottom blue line represent the observed, calculated, and difference patterns, respectively. Vertical green tick bars stand for the Bragg positions. (b) Structure of L-IrS_2 at 300 K. (c) [100] dDPC-STEM image of L-IrS_2, the O1 stacking of the layers remains (the octahedra are traced). (d) Illustration of two IrS_6 polyhedra on both sides of the Van der Waals gap of L-IrS_2. The bi-pyramidal coordination is evidenced as well as the short S-S distances in the interlayer. (e) Magnitude of the Fourier transform of the Ir L_3-edge EXAFS oscillations on L-IrS_2 and model fitting in pink dots and black solid line, respectively. (f) [100] HAADF-STEM image of L-IrS_2. The Ir columns are shifted to form pairs with short projected intercolumn distances of ~2.5 Å and long projected distances of ~3.2 Å between the pairs.

Altogether, structural analyses showed that the S-S dimers are preserved during the initial uptake of Li in J-IrS_2 but are broken afterwards at high Li uptake as the lithium conversion reaction proceeds. On the other hand, L-LiIrS_2 preserved the layered structure upon delithiation and the L-IrS_2 exhibits distorted Ir-S_{5+1} square pyramids (instead of Ir-S_6 octahedra) with short Ir-Ir distances in between. Therefore, the structural evolutions of J-IrS_2 and L-LiIrS_2 are completely different from one another and the remaining question is about the charge compensation mechanism (redox centers) in both these materials.

D) Charge compensation mechanisms

The evolution of the redox states of the iridium atoms in L-$LiIrS_2$, L-IrS_2, J-$Li_{0.5}IrS_2$ and J-IrS_2 was first investigated via Ir L_3-edge XAS (cf. figure 6a). At first sight the absorption spectrum shape for the four samples, look similar with only slight changes in the white line that could be indicative of different Ir environments. Hence, a small shift of the edge position can be seen in the following order E(L-$LiIrS_2$) > E(L-IrS_2) = E(J-$Li_{0.5}IrS_2$) > E(J-IrS_2) that could be attributed to a slight electron density changes around this atom associated to a modification of the iono-covalency of the Ir-S bonds. To get deeper insights, iridium 4f XPS spectra were collected and the $4f_{7/2}$-$4f_{5/2}$ spin orbit components of J-$Li_{0.5}IrS_2$, J-IrS_2, L-IrS_2, and L-$LiIrS_2$ are shown in Figure 6b. Globally, all compounds show similar binding energy (61.7 eV for $4f_{7/2}$) at the exception of the one of L-$LiIrS_2$ that is slightly lower (60.9 eV for $4f_{7/2}$), indicative of a comparatively lower ionization state for iridium. Moreover, each $4f_{7/2}$ and $4f_{5/2}$ component (L-$LiIrS_2$ in Figure 6b) displays a fine structure with a shoulder at higher binding energy. We should note that this fine structure is not due a priori to the coexistence of two oxidation states of iridium, but rather to a multi-electron process inherent in photoemission spectroscopy, which is often observed for transition metals. For example, the Ir 4f spectrum of Li_2IrO_3 displays the same shape, although it is composed of a unique 4+ oxidation state of iridium in a unique environment.[34] Since this kind of fine structure is closely linked to the local environment of the probed atom, and therefore to the structure, the disappearance of this shouldering when moving from L-$LiIrS_2$ to the delithiated phase L-IrS_2 is in good agreement with our SXRD/STEM results showing a significant change of crystalline structure upon Li extraction. Finally, SQUID measurements on both J-IrS_2 and L-IrS_2 (cf. figure S14) indicates diamagnetic behavior for both these compounds. All these observations are consistent with an Ir^{3+} (i.e. a d^6 low spin electronic configuration) with likely an effective charge (ionization degree) slightly lower for Ir in L-$LiIrS_2$. This indicates that while iridium is involved in the electrochemical processes of these compounds its contribution remains low and naturally questions the presence of another redox center.

Sulfur 2p XPS spectra were equally collected for the same four compositions (figure 6c). The J-IrS_2 spectrum can be decomposed in two components of similar intensities, the first one at low binding energy (S $2p_{3/2}$ at 161.8 eV) accounting for S^{2-} species and the second one at higher binding energy (163.4 eV) indicating oxidized sulfur species that can be unambiguously attributed to the $(S_2)^{n-}$ ($n \approx 2$) dimers observed in the structure. Upon lithium insertion (J-$Li_{0.5}IrS_2$) a significant (50%) drop of the $(S_2)^{n-}$ intensity to the benefit of S^{2-} is observed which confirms that the reduction of J-IrS_2 into J-$Li_{0.5}IrS_2$ involves mainly sulfur redox.

Moving to the layered structures, the S 2p XPS spectrum of L-LiIrS_2 shows principally S^{2-} contribution (161.8 eV), with in addition a contribution at higher binding energy (162.8 eV). Note that the binding energy is different from $(S_2)^{n-}$ observed in J-IrS_2 phase and is attributed to oxidized sulfur specie S^{m-} (m<2) that is different from S-S dimer. The presence of S^{m-} can be due to the Li/Ir off-stoichiometry of the pristine compound (estimated Li/Ir = 0.9, see above) and such average charge of the sulfur atoms lower than -2 is coherent with the relatively low c/a ratio calculated for the L-LiIrS_2 structure. This low c/a ratio might also be directly related to a partial depletion of the sp anionic band (less repulsive S…S interactions) associated with the S^{m-} (m<2) electronic configuration of sulfur anions. This is also coherent with the lower ionization degree of Ir in L-LiIrS_2 previously discussed. Moreover, a slight contribution of elemental sulfur is also observed (at 164.1 eV), possibly assigned to unreacted sulfurs at the particle surface. While removing the lithium, the relative intensity of the S^{m-} peak increased compared to that of the S^{2-} (with in addition, in a smaller extent, the increase of the elemental sulfur contribution at higher binding energy). These results demonstrate the strong implication of the sulfur in the L-LiIrS_2/L-IrS_2 redox process, which is in line with bond valence sum calculations, indicating that L-IrS_2 is composed of sulfur atoms with two different charges referred to as S1 and S2 (see table S7), with the latter being more oxidized. However, it is worth noticing that the binding energy of the oxidized S atoms in L-IrS_2 is very different from the $(S_2)^{n-}$ (n≈2) dimers in J-IrS_2, which suggests different oxidized species in line with SXRD/STEM analyses based on the S-S distances being too long (2.9 Å) to account for a S-S chemical bond in layered IrS_2. To further interrogate the nature of the oxidized sulfur species for these systems, Raman spectra of the four compounds have been collected and the results are represented in figure 6e.

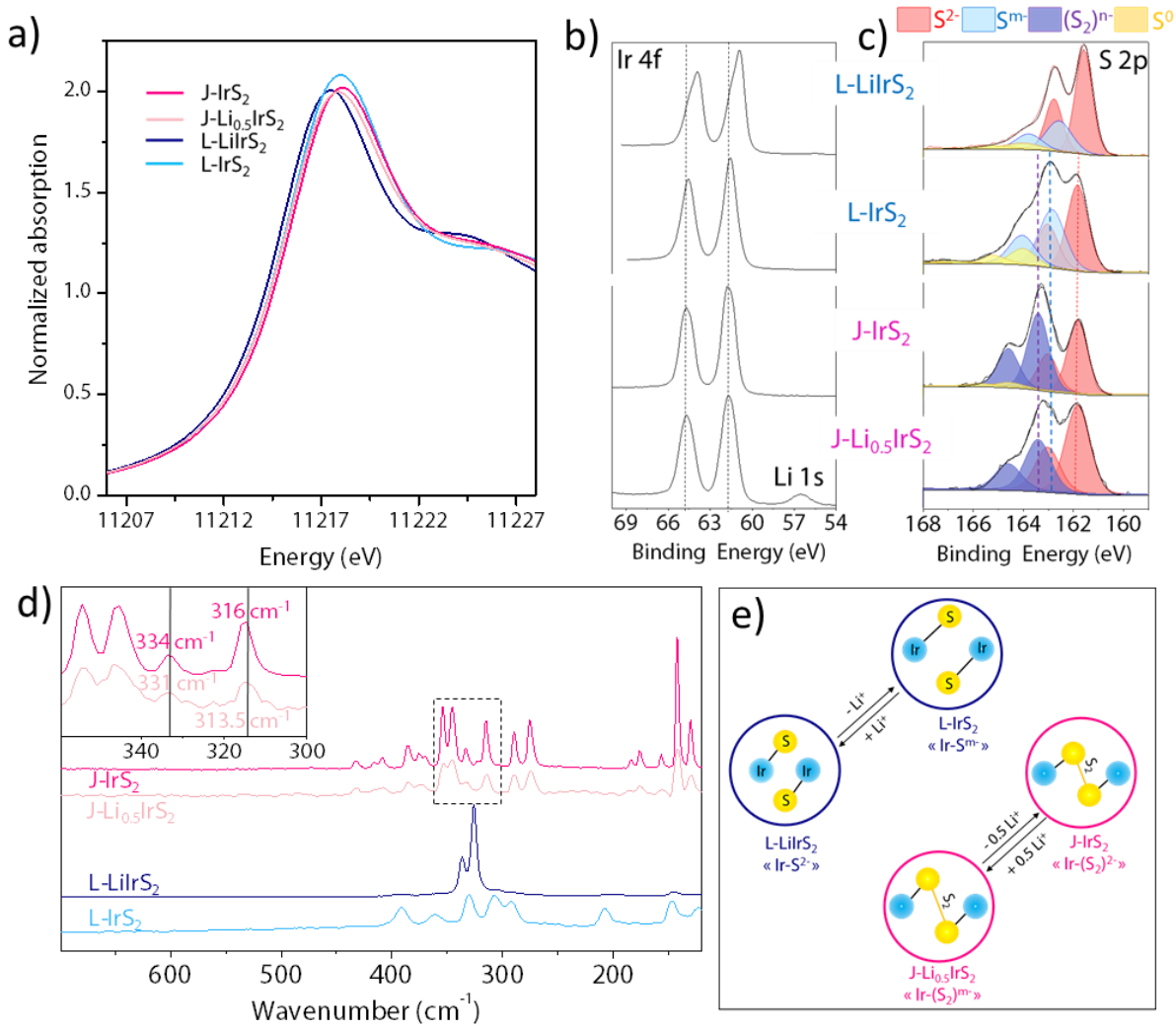

Figure 6: a) X-ray absorption near-edge structure of four Li_xIrS_2 compounds at Ir L_3-edge. b- c) Ir 4f and S 2p XPS spectra. The Li 1s component observed besides the Ir 4f spectrum of J-$Li_{0.5}IrS_2$ mostly corresponds to residues at the surface originating from the chemical lithiation reaction used to synthetize this compound. The S 2p spectra have been decomposed in several components: S^{2-}, S^{m-}, $(S_2)^{n-}$ dimers, and a surface contribution of elemental sulfur S^0. e) Raman spectra of the four Li_xIrS_2. The inset is a zoom in the [360 cm^{-1}-300 cm^{-1}] region where the positions of the two peaks attributed to the S-S dimer stretching are given for both J-IrS_2 and J-$Li_{0.5}IrS_2$. f) Schematic drawing of the charge compensation in both J- and L-Li_xIrS_2 polymorphs.

The Raman spectrum measured for J-IrS_2 shows peaks related to the $(S_2)^{n-}$ (n≈2) stretching modes at 334 and 316 cm^{-1}, indicating a 55 to 65 $N.m^{-1}$ bonding strength between the two sulfur atoms. Upon insertion of 0.5 Li, the overall structure of the Raman spectrum is conserved in spite of some peaks shifts. In particular the peaks related to the S-S dimers stretching are still present but they have broadened and shifted towards lower energies (331 and 313.5 cm^{-1}) indicating the retention of the S-S bond, which are however slightly weakened (50 to 60 $N.m^{-1}$). Such softening of the dimers corresponds to an elongation of 1 or 2 % of the S-S bonds, which is in agreement with our structural findings. At first sight such elongation of the dimer is consistent with an electrochemical reduction of

this entity, however, one would expect a more significant distortion for the transition from $(S_2)^{2-}$ to $(S_2)^{3-}$. Nevertheless, it is important to remember that these materials are highly covalent, the electronic levels of $(S_2)^{2-}$ of J-IrS_2 are likely strongly hybridized with the iridium ones and therefore the charge carried by the sulfur dimer is strongly delocalized explaining this small length variations. It is also possible that the structure of the material itself constrains the elongation of the dimer. At this stage, one could argue that a global reduction of the $(S_2)^{2-}$ to $(S_2)^{3-}$ contrasts with the XPS results since under such a scenario a shift to lower biding energy of the $(S_2)^{2-}$ signal in the J-$Li_{0.5}IrS_2$ S2p spectrum is expected. However, we solely observe a change in the $(S_2)^{2-}/S^{2-}$ signal intensities ratio. Such apparent contradiction can be reconciled by considering the $(S_2)^{3-}$ dimer as an entity evolving dynamically between $(S_2)^{2-}$ and S^{2-} . Therefore, it would be tempting to talk, alike in organic chemistry, of mesomery with the resonance forms being: $(S_2)^{3-} = [(S_2)^{2-} \leftrightarrow S^{2-}]$. Such a dynamic scenario could also explain in part the difficulties encountered for the theoretical simulation of these phases.

In contrast, the Raman spectra collected for the layered systems drastically differ between L-LiIrS_2 and L-IrS_2. The L-LiIrS_2 Raman spectrum ($P\bar{3}m1$) shows only two peaks (associated to A_{1g} and E_g modes) in contrast to the one of L-IrS_2 that is more complex. This difference is coherent with the symmetry lowering observed through delithiation of L-LiIrS_2, hence further supporting the existence of structural distortions in the material as previously described. However, further force field analysis would be needed to make proper attribution of the spectrum peaks.

Altogether these results provide an insight in the charge compensation mechanism and its interplay with the electronic structure evolution of the materials. According to the density of states of J-IrS2 and considering a rigid band structure, the insertion of electrons in J-IrS_2 is expected to progressively fill the antibonding states of the S-S dimer hybridized with both Iridium and S^{2-} sulfur (cf. figure S15). This will first lead to a softening of the S-S bond (J-$Li_{0.5}IrS_2$) and ultimately to its breaking (J-LiIrS_2). However, this simple band picture does not explain the voltage drop at x = 0.5. To gain further insight into this aspect, Galvanostatic Intermittent Titration Technique (GITT) measurements were conducted. (cf. figure S16). They reveal a small relaxation voltage through the J-$Li_{0.5}IrS_2$ formation plateau as opposed to a strong one for the second plateau corresponding to the J-LiIrS_2 formation, but interestingly the relaxed voltage barely changes from J-$Li_{0.5}IrS_2$ to J-LiIrS_2. These implies that the phases should form at nearly the same potential but this does not happen due to different kinetics. This kinetic limitation can be rationalized based on structural consideration by recalling that all empty ramsdelite octahedral sites are filled with lithium in J-$Li_{0.5}IrS_2$ with additionally the blocking of the rutile type-sites by S-S dimers. Thus, to uptake further Li, the structure of J-$Li_{0.5}IrS_2$ reorganizes via the breaking of the dimers and this comes with a kinetic penalty.

The charge compensation in L-IrS_2 appears more complicated although some insights can be obtained in light of reported studies on $IrTe_2$. This compound adopts a room temperature O1 layered structure made of perfectly regular $IrTe_6$ octahedra but shows a distorted O1 layer structure at low temperature with Ir-Ir dimerization, hence bearing some resemblance to L-IrS_2. A multicenter bond involving the iridium atoms pertaining to the dimers and the tellurium atoms joining these two iridium atoms has been proposed to account for the low temperature Ir-Ir dimerization. Thus, by analogy, the reorganization of the electronic structure in L-IrS_2 could stabilize the oxidized sulfur atoms. However, at this stage DFT calculations are strongly needed to rationalize such hypothesis and preliminary attempts have not yet been conclusive.

Finally, it is important to mention that Li_xIrS_2 is highly covalent system and is not possible to attribute a formal charge to the iridium and sulfur or to classify the redox process as strictly "cationic" or "anionic". However, the main conclusion of this charge compensation study is that the L- and J-polymorphs follow completely different redox pathways (cf. figure 6f). The J- system involves an Ir-$(S_2)^{n-}$ entity (n>2) while the layered system involves Ir-S^{m-} entity (m < 2) in the redox process; here the prefix "Ir" suggests that the anionic levels involved in the redox are strongly hybridized by the Iridium. However, for simplification purpose, the redox couple of the J and L- system are mentioned as $(S_2)^{n-}/(S_2)^{2-}$ and S^{m-}/S^{2-} respectively in the following discussion.

Discussion and conclusion

Altogether, we studied the Li-reactivity of two IrS_2 polymorphs; the J-IrS_2 one synthesized at high temperature having S-S dimers and the L-IrS_2 obtained by delithiating layered $LiIrS_2$ having oxidized sulfur but no S-S dimers. Spectroscopic analyses unambiguously demonstrated that both polymorphs followed different charge compensation mechanisms through cycling. Such specific features of two polymorphs that react with Li^+ via two different redox couples makes the IrS_2 system unique to understand the structure - charge compensation mechanism interlink.

Electrochemical reactions proceed at room temperature and usually lead to metastable phases. However, the thermodynamic reversible path for lithiation and delithiation of J-IrS_2 and L-Li_xIrS_2 can be identified by conducting reactions at higher temperatures (cf. figure 7 a). By reacting J-IrS_2 with metallic lithium at 600 °C we could produce L-$LiIrS_2$ for Li/Ir = 1 that could then be delithiated by an iodine (I_2) treatment at 900°C to produce J-IrS_2, hence a different reaction lithiation-delithiation pathway from the room temperature electrochemical one. These results indicate that the thermodynamically driven reaction path can be written as:

$$J\text{-}IrS_2 + x\ Li = (1\text{-}x)\ J\text{-}IrS_2 + x\ L\text{-}LiIrS_2 \qquad (1)$$

It is different from the room temperature electrochemical one that follows a kinetic path as schematized in figure 7b. Structurally speaking, the thermodynamic reversible pathway between L-type and J-type is possible only through iridium atoms migration. Though cation migration is often reported in layered materials, studies performed on Li_2IrO_3 demonstrated that the iridium atoms are not likely to migrate during delithiation due to the strongly covalent Ir-O bond.[6,34] On moving from oxides to sulfides, the material becomes even more covalent, hence the migration of Ir is expected to be impeded further. This provides a feasible explanation to account for a different reacting pathway between low and high temperature. Another factor to trigger the J $\Leftrightarrow$ L transition is the breaking and formation of S-S dimers that is associated to electronic rearrangements. Such a strong electronic reorganization is energetically costly and therefore not the most favorable path at low temperature.

Altogether, our results confirm that when activation energies required to form the thermodynamically stable phase are too high, kinetics variables guide the structure selection (i.e. metastable phases) along the phase transformation pathway. More importantly, this reaction pathway selection directly affects the sulfur redox couple. Hence, while thermodynamic path relies on a sulfur redox chemistry enlisting the $(S_2)^{2-}/S^{2-}$ redox couple the room temperature kinetic pathways are constrained to involve metastable sulfur states ($(S_2)^{n-}$ and S^{m-} with n >2 and m<2). Thus, the observed voltages differences (ΔE_J and ΔE_L cf. figure 7 c) between the J and L kinetic pathways and the thermodynamic one are most likely due to the different redox potential associated to these redox couples.

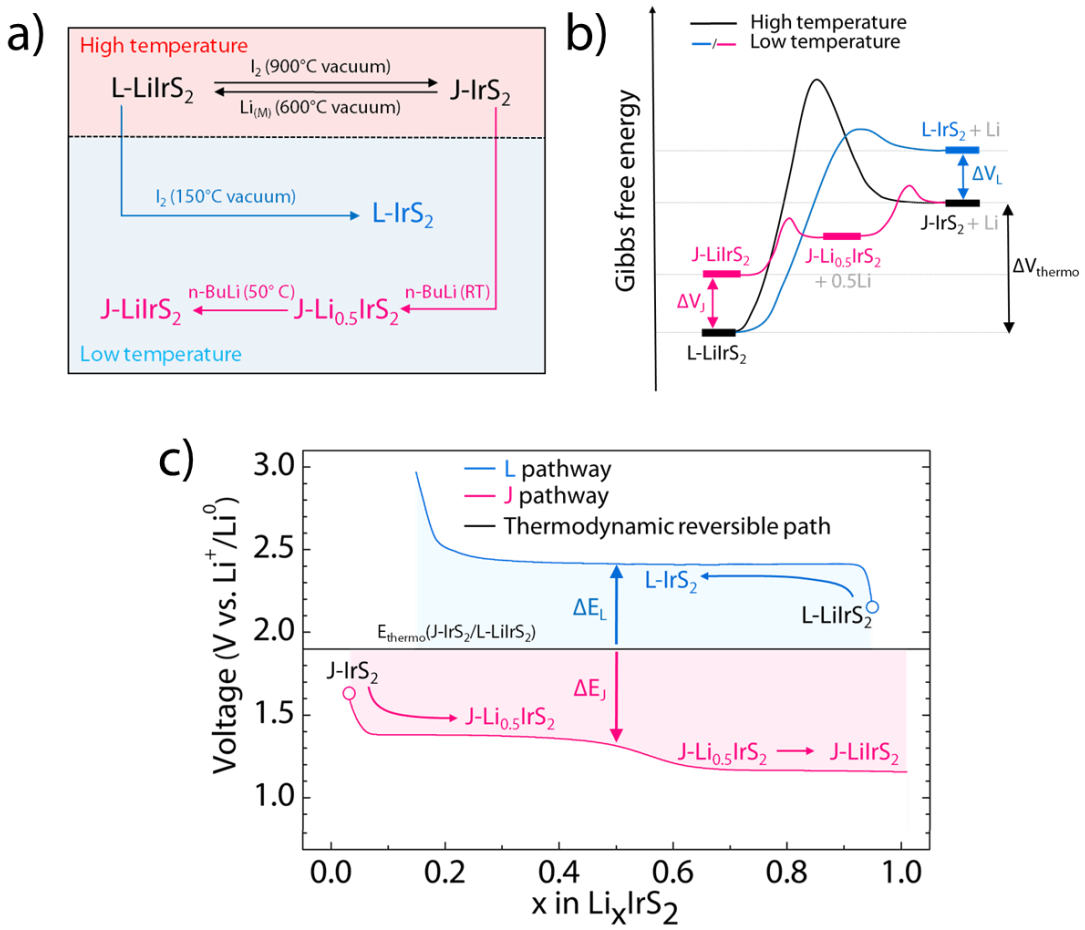

Figure 7: a) Sum up of the chemical lithiation/delithiation products as a function of the reaction temperature. b) Schematic of the energy landscape for the Li_xIrS_2 system. In particular, it highlights the relative stability of the phases and the activation energy associated to all the reactions. c) Comparison between the experimental electrochemical curves obtained for the J and L pathways and the calculated (cf. SI) thermodynamic potential associated to the reaction (1).

Next, a legitimate question arises on how such findings could provide more insights into the electrochemistry of the lithium-rich oxides. To that end, it is interesting to make a parallel between our findings and the hypothesized multistep mechanism for anionic redox materials we earlier proposed based on isothermal calorimetry.[35] This process (cf. figure 8a) consists of decomposing the lithiation/ delithiation to electrochemical steps with less structural/electronic reorganization, followed by chemical rearrangement steps (cation migration, shortening of O-O bonds or even dimer formation according to some authors).

Thus, according to this model, the electrochemical steps, i.e. those that define the potential, are done at a fixed structure. Therefore, similarly to L-$LiIrS_2$ in charge, the withdrawal of lithium from a lithium rich oxide ~~lithium~~ is done without possible migration of transition metals and thus without any O-O dimer formation. On the contrary, after structural reorganization the loaded material contains

migrated cations in the interlayer and according to some authors O-O dimers. Therefore, similarly to the Li insertion in J-IrS_2, the redox couple involved in the discharge of the lithium rich oxide must be impacted by the presence of the dimer. Thus, by analogy with the Li_xIrS_2 systems, the charge and discharge in a lithium-rich oxide are likely to occur via two different redox couples, which explains the potential difference, i.e. the hysteresis, observed (cf. figure 8b). It is important to note that the analogy made only allows predicting a difference of redox couple between charge and discharge in no case we affirm that these couples are identical for the oxides and the Li_xIrS_2 system.

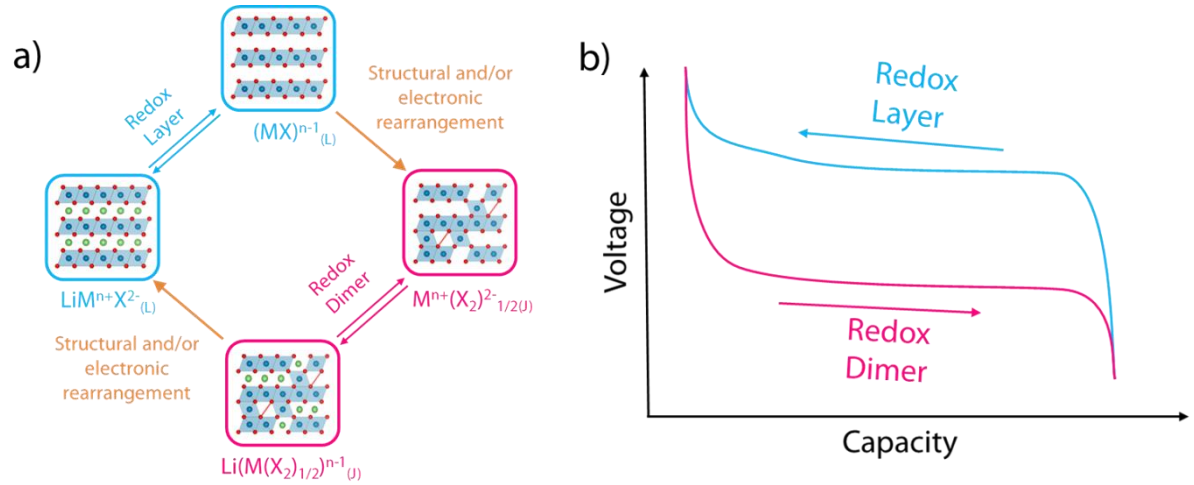

Figure 8: a) Schematic drawing of the proposed reaction pathway within the cycling of anionic redox active material. According to this scenario, the extraction of lithium is done through a first redox process involving the anion and/ or the cation (redox layer). This metastable form then reorganizes chemically to form anionic dimers (X_2). The subsequent electrochemical process for lithium intercalation then involves the redox of the dimer (redox dimer), which at the end of the discharge can reorganizes partly/ fully to reform the pristine like material. b) The resulting (hypothetical) electrochemical curve with hysteresis due to difference in redox couples between charge (layer) and discharge (dimer). The wordings 'layer' and 'dimer' in the figure represents layered structure and the rearranged structure with dimers respectively.

Moreover, such squared mechanism suggests (cf. figure 8 a), at first sight, the feasibility to cure this hysteresis by preventing the reorganization steps. This is what we have realized here by chemically designing these IrS_2 polymorphs since L-IrS_2/L-$LiIrS_2$ and J-IrS_2/J-$Li_{0.5}IrS_2$ anionic redox process occurs without any hysteresis. Accordingly, recent studies have correlated the absence of hysteresis in Li_2IrO_3[36] or $Na_2Mn_3O_7$[37] to the lack of structural evolution concomitantly with the electrochemical reaction.

In summary, we reported the chemical design of novel IrS_2 polymorphs that were used as an ideal system to understand the structurally driven reaction pathways during lithiation/delithiation of anionic redox based compounds. Combined XRD, XPS and Raman revealed that both J-IrS_2 and L-IrS_2 polymorphs, with or without S-S dimers, have asymmetric redox processes involving different reaction

intermediates. Moreover, such tailor-made sulfides have helped in experimentally rationalizing the multistep “square scheme” model previously proposed. This model can extend to most oxides showing anionic redox activity. Apart from providing mechanistic insights, this revisit of the chalcogenide chemistry opens up a new way to predict and chemically design anionic redox based materials with mitigated hysteresis. Lastly, by reporting a new IrS_2 phase we broaden the layered chalcogenides family that constitute a hot topic nowadays owing to unusual catalytic, optical, electronic, and spintronic properties.

Acknowledgement

Use of the 11-BM mail service of the APS at Argonne National Laboratory was supported by the US Department of Energy under contract No. DE-AC02-06CH11357 and is gratefully acknowledged. T.M. acknowledges the Ecole Normale Supérieure Paris-Saclay for his PhD scholarship. The authors acknowledge the staff of the MPBT (physical properties – low temperature) platform of Sorbonne Université for their support. J.-M.T. acknowledges the funding from European Research Council (ERC) (FP/2014)/ERC grant/project no.670116-ARPEMA. XAS experiments were performed on the ROCK beamline (financed by ANR- 10-EQPX-45) at SOLEIL Synchrotron, France.

Conflict of interest

The authors declare no conflict of interest.

Associated Content

*Supporting Information

The Supporting Information containing additional XRD and electron diffraction patterns, crystallographic details and electrochemical analyses is available free of charge on the ACS Publications website.

Corresponding author : Jean-Marie Tarascon (jean-marie.tarascon@college-de-france.fr)

References

(1) Armand, J.-M. T. & M. Issues and Challenges Facing Rechargeable Lithium Batteries. *Nature* **2001**, *414* (November), 359–367. https://doi.org/10.1038/35104644.

(2) Assat, G.; Tarascon, J. M. Fundamental Understanding and Practical Challenges of Anionic Redox Activity in Li-Ion Batteries. *Nat. Energy* **2018**, *3* (5), 373–386. https://doi.org/10.1038/s41560-018-0097-0.

(3) Li, B.; Xia, D. Anionic Redox in Rechargeable Lithium Batteries. *Adv. Mater.* **2017**, *1701054* (1), 1–28. https://doi.org/10.1002/adma.201701054.

(4) Gent, W. E.; Abate, I. I.; Yang, W.; Nazar, L. F.; Chueh, W. C. Ll Perspective Design Rules for High-Valent Redox in Intercalation Electrodes. *Joule* **2020**, 1–29. https://doi.org/10.1016/j.joule.2020.05.004.

(5) Gent, W. E.; Lim, K.; Liang, Y.; Li, Q.; Barnes, T.; Ahn, S.-J.; Stone, K. H.; McIntire, M.; Hong, J.; Song, J. H.; Li, Y.; Mehta, A.; Ermon, S.; Tyliszczak, T.; Kilcoyne, D.; Vine, D.; Park, J.-H.; Doo, S.-K.; Toney, M. F.; Yang, W.; Prendergast, D.; Chueh, W. C. Coupling between Oxygen Redox and Cation Migration Explains Unusual Electrochemistry in Lithium-Rich Layered Oxides. *Nat. Commun.* **2017**, *8* (1), 2091. https://doi.org/10.1038/s41467-017-02041-x.

(6) Hong, J.; Gent, W. E.; Xiao, P.; Lim, K.; Seo, D.; Wu, J.; Csernica, P. M.; Takacs, C. J.; Nordlund, D.; Sun, C.; Stone, K. H.; Passarello, D.; Yang, W.; Prendergast, D.; Ceder, G.; Toney, M. F.; Chueh, W. C. Metal–Oxygen Decoordination Stabilizes Anion Redox in Li-Rich Oxides. *Nat. Mater.* **2019**, *18* (3), 256–265. https://doi.org/10.1038/s41563-018-0276-1.

(7) House, R. A.; Maitra, U.; Pérez-Osorio, M. A.; Lozano, J. G.; Jin, L.; Somerville, J. W.; Duda, L. C.; Nag, A.; Walters, A.; Zhou, K. J.; Roberts, M. R.; Bruce, P. G. Superstructure Control of First-Cycle Voltage Hysteresis in Oxygen-Redox Cathodes. *Nature* **2020**, *577* (7791), 502–508. https://doi.org/10.1038/s41586-019-1854-3.

(8) Jacquet, Q.; Iadecola, A.; Saubanère, M.; Li, H.; Berg, E. J.; Rousse, G.; Cabana, J.; Doublet, M. L.; Tarascon, J. M. Charge Transfer Band Gap as an Indicator of Hysteresis in Li-Disordered Rock Salt Cathodes for Li-Ion Batteries. *J. Am. Chem. Soc.* **2019**, *141* (29), 11452–11464.

https://doi.org/10.1021/jacs.8b11413.

(9) Taylor, Z. N.; Perez, A. J.; Coca-Clemente, J. A.; Braga, F.; Drewett, N. E.; Pitcher, M. J.; Thomas, W. J.; Dyer, M. S.; Collins, C.; Zanella, M.; Johnson, T.; Day, S.; Tang, C.; Dhanak, V. R.; Claridge, J. B.; Hardwick, L. J.; Rosseinsky, M. J. Stabilization of O.O Bonds by D0 Cations in Li4+xNi1-XWO6 (0 ≤ x ≤ 0.25) Rock Salt Oxides as the Origin of Large Voltage Hysteresis. *J. Am. Chem. Soc.* **2019**, *141* (18), 7333–7346. https://doi.org/10.1021/jacs.8b13633.

(10) Grimaud, A.; Iadecola, A.; Batuk, D.; Saubanère, M.; Abakumov, A. M.; Freeland, J. W.; Cabana, J.; Li, H.; Doublet, M. L.; Rousse, G.; Tarascon, J. M. Chemical Activity of the Peroxide/Oxide Redox Couple: Case Study of Ba5Ru2O11 in Aqueous and Organic Solvents. *Chem. Mater.* **2018**, *30* (11), 3882–3893. https://doi.org/10.1021/acs.chemmater.8b01372.

(11) Jobic, S.; Deniard, P.; Brec, R.; Rouxel, J.; Drew, M. G. B.; David, W. I. F. Properties of the Transition Metal Dichalcogenides: The Case of IrS2 and IrSe2. *J. Solid State Chem.* **1990**, *89*, 315–327. https://doi.org/10.1016/0022-4596(90)90273-Z.

(12) Jellinek, F. *Inorganic Sulfur Chemistry*; Nickless, G., Ed.; Elsevier. Amsterdam, 1968.

(13) Gide, A. 済無No Title No Title No Title. *Angew. Chemie Int. Ed. 6(11), 951–952.* **1967**, *7*, 5–24.

(14) Rouxel, J. Anion-Cation Redox Competition and the Formation of New Compounds in Highly Covalent Systems. *Chem. - A Eur. J.* **1996**, *2* (9), 1053–1059. https://doi.org/10.1002/chem.19960020904.

(15) Tomczuk, Z.; Tani, B.; Otto, N. C.; Roche, M. F.; Vissers, D. R. Phase Relationships in Positive Electrodes of High Temperature Li - Al / LiCl - KCl / FeS2 Cells. *J. Electrochem. Soc.* **1982**, *129* (5), 925–931. https://doi.org/10.1149/1.2124067.

(16) Shao-horn, Y.; Osmialowski, S.; Horn, Q. C. Reinvestigation of Lithium Reaction Mechanisms in FeS 2 Pyrite at Ambient Temperature. *J. Electrochem. Soc.* **2002**, 1547–1555. https://doi.org/10.1149/1.1516772.

(17) Butala, M. M.; Mayo, M.; Doan-Nguyen, V. V. T.; Lumley, M. A.; Göbel, C.; Wiaderek, K. M.; Borkiewicz, O. J.; Chapman, K. W.; Chupas, P. J.; Balasubramanian, M.; Laurita, G.; Britto, S.; Morris, A. J.; Grey, C. P.; Seshadri, R. Local Structure Evolution and Modes of Charge Storage in Secondary Li–FeS 2 Cells. *Chem. Mater.* **2017**, *29* (7), 3070–3082. https://doi.org/10.1021/acs.chemmater.7b00070.

(18) Sourisseau, C.; Cavagnat, R.; Fouassier, M.; Jobic, S.; Deniard, P.; Brec, R.; Rouxel, J. The

Vibrational Resonance Raman Spectra and the Valence Force Field of Iridium Dichalcogenides, IrS2 and IrSe2. *J. Solid State Chem.* **1991**, *91* (1), 153–172. https://doi.org/10.1016/0022-4596(91)90069-T.

(19) Leriche, J. B.; Hamelet, S.; Shu, J.; Morcrette, M.; Masquelier, C.; Ouvrard, G.; Zerrouki, M.; Soudan, P.; Belin, S.; Elkaïm, E.; Baudelet, F. An Electrochemical Cell for Operando Study of Lithium Batteries Using Synchrotron Radiation. *J. Electrochem. Soc.* **2010**, *157* (5), A606. https://doi.org/10.1149/1.3355977.

(20) Frontzek, M. D.; Whitfield, R.; Andrews, K. M.; Jones, A. B.; Bobrek, M.; Vodopivec, K.; Chakoumakos, B. C.; Fernandez-Baca, J. A. WAND 2 —A Versatile Wide Angle Neutron Powder/Single Crystal Diffractometer. *Rev. Sci. Instrum.* **2018**, *89* (9), 092801. https://doi.org/10.1063/1.5033900.

(21) Rodríguez-Carvajal, J. Recent Advances in Magnetic Structure Determination by Neutron Powder Diffraction. *Phys. B Phys. Condens. Matter* **1993**, *192* (1–2), 55–69. https://doi.org/10.1016/0921-4526(93)90108-I.

(22) Adams, S. From Bond Valence Maps to Energy Landscapes for Mobile Ions in Ion-Conducting Solids. *Solid State Ionics* **2006**, *177* (19-25 SPEC. ISS.), 1625–1630. https://doi.org/10.1016/j.ssi.2006.03.054.

(23) Adams, S. Practical Considerations in Determining Bond Valence Parameters. *Struct. Bond.* **2014**, *158*, 91–128. https://doi.org/10.1007/430_2013_96.

(24) Briois, V.; La Fontaine, C.; Belin, S.; Barthe, L.; Moreno, T.; Pinty, V.; Carcy, A.; Girardot, A.; Fonda, E. ROCK: The New Quick-EXAFS Beamline at SOLEIL. *J. Phys. Conf. Ser.* **2016**, *712*, 012149. https://doi.org/10.1088/1742-6596/712/1/012149.

(25) Ravel, B.; Newville, M. ATHENA , ARTEMIS , HEPHAESTUS : Data Analysis for X-Ray Absorption Spectroscopy Using IFEFFIT. *J. Synchrotron Radiat.* **2005**, *12*, 537–541. https://doi.org/10.1107/S0909049505012719.

(26) Levi, E.; Zinigrad, E.; Teller, H.; Levi, M. D.; Aurbach, D. The Structure of a 3 V Li x MnO2 Cathode and Its Change upon Electrochemical Lithiation. *J. Electrochem. Soc.* **1998**, *145* (10), 3440–3443. https://doi.org/10.1149/1.1838824.

(27) Boultif, A.; Loueer, D. Indexing of Powder Diffraction Patterns for Low-Symmetry Lattices by the Successive Dichotomy Method. *J. Appl. Crystallogr.* **1991**, *24* (pt 6), 987–993.

https://doi.org/10.1107/S0021889891006441.

(28) Boultif, A. History of the Dichotomy Method for Powder Pattern Indexing. *Powder Diffr.* **2005**, *20* (04), 284–287. https://doi.org/10.1154/1.2135307.

(29) Mendiboure, A.; Delmas, C.; Hagenmuller, P. Electrochemical Intercalation and Deintercalation of NaxMnO2 Bronzes. *J. Solid State Chem.* **1985**, *57* (3), 323–331. https://doi.org/10.1016/0022-4596(85)90194-X.

(30) Goodenough, J. B.; Kim, Y. Locating Redox Couples in the Layered Sulfides with Application to Cu[Cr2]S4. *J. Solid State Chem.* **2009**, *182* (10), 2904–2911. https://doi.org/10.1016/j.jssc.2009.08.005.

(31) Saleh, G.; Artyukhin, S. First-Principles Theory of Phase Transitions in IrTe2. *J. Phys. Chem. Lett.* **2020**, *11* (6), 2127–2132. https://doi.org/10.1021/acs.jpclett.0c00012.

(32) Oh, Y. S.; Yang, J. J.; Horibe, Y.; Cheong, S. W. Anionic Depolymerization Transition in IrTe2. *Phys. Rev. Lett.* **2013**, *110* (12), 1–5. https://doi.org/10.1103/PhysRevLett.110.127209.

(33) Joseph, B.; Bendele, M.; Simonelli, L.; Maugeri, L.; Pyon, S.; Kudo, K.; Nohara, M.; Mizokawa, T.; Saini, N. L. Local Structural Displacements across the Structural Phase Transition in IrTe2 : Order-Disorder of Dimers and Role of Ir-Te Correlations. *Phys. Rev. B* **2013**, *224109*, 3–6. https://doi.org/10.1103/PhysRevB.88.224109.

(34) Pearce, P. E.; Perez, A. J.; Rousse, G.; Saubanère, M.; Batuk, D.; Foix, D.; McCalla, E.; Abakumov, A. M.; Van Tendeloo, G.; Doublet, M. L.; Tarascon, J. M. Evidence for Anionic Redox Activity in a Tridimensional-Ordered Li-Rich Positive Electrode β-Li2IrO3. *Nat. Mater.* **2017**, *16* (5), 580–586. https://doi.org/10.1038/nmat4864.

(35) Assat, G.; Glazier, S. L.; Delacourt, C.; Tarascon, J.-M. Probing the Thermal Effects of Voltage Hysteresis in Anionic Redox-Based Lithium-Rich Cathodes Using Isothermal Calorimetry. *Nat. Energy* **2019**, *4* (8), 647–656. https://doi.org/10.1038/s41560-019-0410-6.

(36) Kitchaev, D. A.; Vinckeviciute, J.; Van Der Ven, A. Delocalized Metal-Oxygen π-Redox Is the Origin of Anomalous Nonhysteretic Capacity in Li-Ion and Na-Ion Cathode Materials. *J. Am. Chem. Soc.* **2021**, *143* (4), 1908–1916. https://doi.org/10.1021/jacs.0c10704.

(37) Tsuchimoto, A.; Shi, X. M.; Kawai, K.; Mortemard de Boisse, B.; Kikkawa, J.; Asakura, D.; Okubo, M.; Yamada, A. Nonpolarizing Oxygen-Redox Capacity without O-O Dimerization in Na2Mn3O7. *Nat. Commun.* **2021**, *12* (1), 1–7. https://doi.org/10.1038/s41467-020-20643-w.